Low-frequency wave-energy amplification in graded two-dimensional resonator arrays

Luke G. Bennetts[1], Malte A. Peter[2,3], Richard V. Craster[4]

[1]School of Mathematical Sciences, University of Adelaide, Adelaide, SA 5005, Australia

[2]Institute of Mathematics, University of Augsburg, 86135 Augsburg, Germany

[3]Augsburg Centre for Innovative Technologies, University of Augsburg, 86135 Augsburg, Germany

[4]Department of Mathematics, Imperial College London, South Kensington Campus, London, SW7 2AZ, UK

June 28, 2019

Abstract

Energy amplification in square-lattice arrays of C-shaped low-frequency resonators, where the resonator radii are graded with distance, is investigated in the two-dimensional linear acoustics setting for both infinite (in one dimension) and finite arrays. Large amplifications of the incident energy are shown in certain array locations. The phenomenon is analysed using: (i) band diagrams for doubly-periodic arrays; (ii) numerical simulations for infinite and finite arrays; and (iii) eigenvalue analysis of transfer matrices operating over individual columns of the array. It is shown that the locations of the large amplifications are predicted by propagation cut-offs in the modes associated to the transfer-matrix eigenvalues. For the infinite array, the eigenvalues form a countable set, and for the low frequencies considered, only a single propagating mode exists for a given incident wave, which cuts off within the array, leading to predictive capabilities for the amplification location. For the finite array, it is shown that (in addition to a continuous spectrum of modes) multiple discrete propagating modes can be excited, with the grading generating new modes, as well as cutting others off, leading to complicated amplification patterns. The numerical simulations reveal the largest amplifications are achieved for a single row array, with amplifications an order of magnitude smaller for the corresponding infinite array.

1   Introduction

Recently, [1] have shown that C-shaped bottom-mounted cylinders act as local low-frequency (sub-wavelength) resonators in a line array subject to plane incident waves. A spatial grading of the cylinder radii led to a structure amplifying the incident wave energy by factors up to more than 500—over 11 times greater than the amplification in an isolated cylinder—and over a broad range of wavelengths, with the position of the largest amplification in the array depending on the incident wavelength. The effect is known as rainbow trapping after [2] who illustrated, in optics, how grading the material properties of a tapered waveguide could lead to spatial separation of its spectrum and trapping of the wave; subsequently this idea has been used to advantage in many areas of wave physics, e.g. acoustics [3], elastic waves [4], and plasmonics [5], among others. To illustrate this effect, following [1], Figure 1 shows the energy, E, normalised to unit incident energy for a graded row of ten C-shaped resonators and an incident wavenumber close to the resonant wavenumber of the fifth resonator (counted from the left). The maximum energy amplification occurs in the fourth cylinder; it is > 270 times greater than the incident wave energy, and 6.9 times the amplification in the isolated cylinder.

While the results given in [1] were in the three-dimensional water-wave context, motivated by supplying design ideas for wave-energy-conversion structures, the results can be directly interpreted in a two-dimensional acoustics setting, which will be considered in what follows. Here, the field satisfies
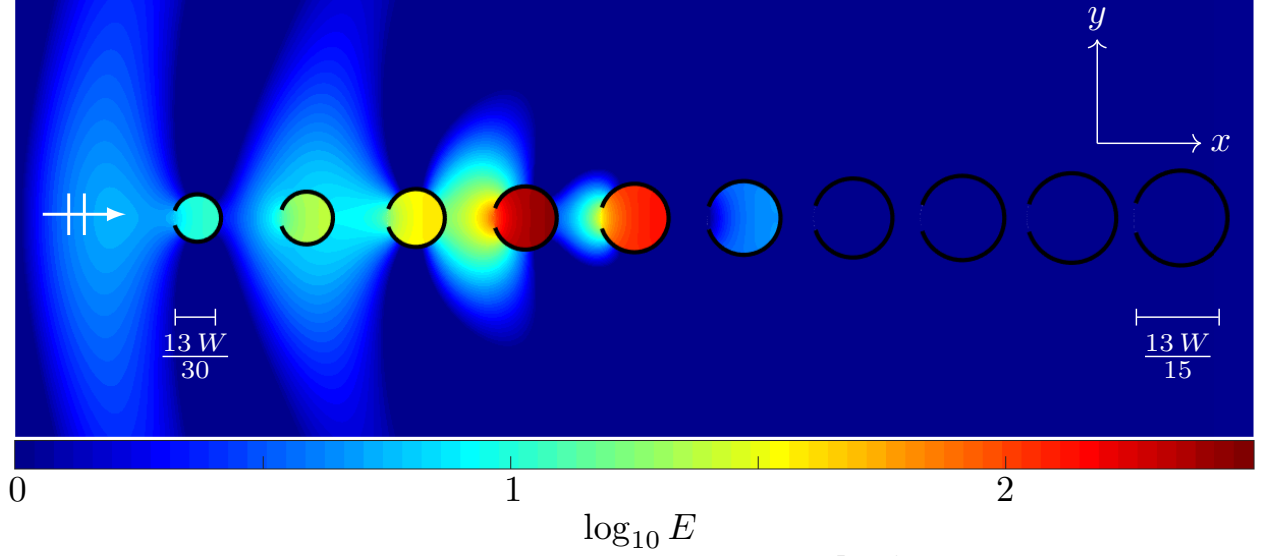
1

Figure 1: Logarithm of normalised energy (unit incident energy) along a single graded row of 10 C-shaped resonators for $a_m / a_1 = (m + 8) / 9$, $a_1 / W = 0.217$, $\varphi = 0.1\,\pi$, $k\,W = 0.476\,\pi$ and $\psi = 0$

the Helmholtz equation (with wavenumber k) in the $\mathbf{x} = (x, y)$-plane, and the C-shapes are sound-hard structures (i.e. homogeneous Neumann conditions are assumed on their surfaces). More precisely, the C-shapes are defined by

$$\mathcal{C}_m = \{\mathbf{x} : (x - x_m)^2 + y^2 = a_m^2, \, \arctan(y/(x - x_m)) < \pi - \varphi\} \quad \text{for} \quad m = 1, \ldots, M, \tag{1}$$

where $M = 10$, $(x_m, 0)$ is the centre location of the mth C-shape, $W = x_{m+1} - x_m$ is the constant spacing (centre to centre), a_m is the radius of the mth C-shape, and φ is the half-angle of its opening (identical for all C-shapes), with the openings at the left-hand end and symmetric about the line $y = 0$, as shown in Figure 1. Correspondingly, the Helmholtz equation is imposed in $\mathbb{R}^2 \setminus \bigcup_m \overline{\mathcal{C}_m}$. Motions are forced by a plane incident wave, with velocity potential

$$\phi_{\text{inc}}(\mathbf{x}) = \mathrm{e}^{\mathrm{i}\,k\,(x\cos\psi + y\sin\psi)}, \tag{2}$$

where ψ is the incident wave direction with respect to the positive x-axis ($\psi = 0$ corresponds to head-on incidence, as in Fig. 1). The system is completed by the Sommerfeld radiation condition as well as a condition ensuring the correct singularity at the tips of the C-shapes.

It was shown in [1] that the rainbow-trapping effect is explained by the behaviour of local Rayleigh–Bloch waves excited in the array. The C-shape-radius grading causes the rightward-propagating Rayleigh–Bloch wave excited at the leading end of the array to slow down progressively along the array, until it reaches a turning point, at which the group velocity is zero. In the language of waveguide modes, at this point, the wave is cut-off and ceases to propagate. The energy carried by the local Rayleigh–Bloch wave accumulates at the turning point, thereby generating large amplifications.

Graded two-dimensional arrays of structures have been shown to support rainbow trapping. In an acoustic setting, [6] showed that a graded array of ordinary cylinders (non-resonant closed circles; in the context introduced above, a zero opening angle, $\varphi = 0$), with lattice spacing decreasing in the direction of the incident wave, can be used to amplify acoustic pressure in certain regions. They showed this experimentally but also argued that the effect is due to the incident wave reaching a region inside the grating where its effective group velocity vanishes so that the incident energy accumulates. Band-structure calculations were used to support this argument.

2

The present work is an extension of [1] to two-dimensional graded arrays on square lattices, in which the locations of the C-shapes are

$$\mathcal{C}_{m,n} = \{\mathbf{x} : (x - x_m)^2 + (y - y_n)^2 = a_m^2, \arctan((y - y_n)/(x - x_m)) < \pi - \varphi\} \qquad (3)$$

for $m = 1, \ldots, M$ and $n = 1, \ldots, N$, where $W = x_{m+1} - x_m = y_{n+1} - y_n$. It can also be viewed as an extension of [6] to resonating members with grading in terms of the resonance properties. Section 2 presents band structures of doubly-periodic arrays of C-shaped resonators, from which the effects of grading can be inferred. Section 3 considers effects of grading for stacks of diffraction gratings, where each grating contains an infinite number of identical C-shaped resonators arranged periodically in a single column. A transfer-matrix method is outlined and the grading effects are related to changes in the spectrum of the underlying (discrete) transfer operator. Section 4 considers the associated finite-array problem, in which each diffraction grating is truncated to contain only a finite number of identical C-shaped resonators. An analogous transfer-matrix method is employed, which is now based on discretisation of a transfer operator associated with a continuum of directions. Section 5 ends the paper with a short summary and brief discussion of the findings.

2   Band diagrams

In order to understand the behaviour of waves travelling through a graded two-dimensional array of structures on a square lattice, it is enlightening to consider the periodic case—a so-called doubly-periodic array, i.e. no grading—the idea being that, as long as the grading is weak enough, the structure will approximately experience a wave field as if it were a member in a periodic array of (global) periodicity equal to the actual local periodicity.

In the periodic case, the problem reduces to finding solutions satisfying the Bloch condition

$$\phi(\mathbf{x} + \mathbf{R}) = e^{i\mathbf{q} \cdot \mathbf{R}} \phi(\mathbf{x}), \qquad (4)$$

for all lattice vectors $\mathbf{R} = (m_1 W, m_2 W)$, where m_1 and m_2 are integers and $\mathbf{q} = (q_1, q_2)$ is the Bloch wave vector, which is part of the unknowns. This problem can be written as an eigenvalue problem with quasi-periodic boundary conditions on the unit cell $(-W/2, W/2)^2$. More precisely, the wavenumber in the Helmholtz equation is now the (square-root of the) eigenvalue of the Laplacian subject to (Floquet–)Bloch conditions at the sides of the unit cell, which are given by

$$\left.\begin{aligned} \phi(W/2, y) &= e^{iq_1 W} \phi(-W/2, y) \\ \partial_x \phi(W/2, y) &= e^{iq_1 W} \partial_x \phi(-W/2, y) \end{aligned}\right\} \quad |y| < W/2, \qquad (5a)$$

and

$$\left.\begin{aligned} \phi(x, W/2) &= e^{iq_2 W} \phi(x, -W/2) \\ \partial_y \phi(x, W/2) &= e^{iq_2 W} \partial_y \phi(x, -W/2) \end{aligned}\right\} \quad |x| < W/2, \qquad (5b)$$

as well as the (unchanged) homogeneous Neumann condition on the C-shape surface.

As we are interested in propagating waves, only real-valued entries of $\mathbf{q}$ are considered. Moreover, by periodicity, it suffices to consider values of $\mathbf{q}$ in the so-called first Brillouin zone $\{\mathbf{q} W \mid \mathbf{q} W \in [-\pi, \pi)^2\}$. In fact, owing to the symmetry of the C-shapes about the x-axis, q_2 is symmetric about the q_1-axis and, by a time-reversal argument, the eigenvalue also does not change if $\mathbf{q}$ is swapped for $-\mathbf{q}$. The full picture is thus given by $\{\mathbf{q} W \mid \mathbf{q} W \in [0, \pi)^2\}$, which makes up the so-called irreducible Brillouin zone in this case.

We solve the Bloch problem using the finite element method. In order to simplify the numerical computation, we add a small thickness to the C-shaped walls. Thus, the radius in the following results refers to the inner radius (decisive for the internal resonance). Results for the fifth C-shape (radius
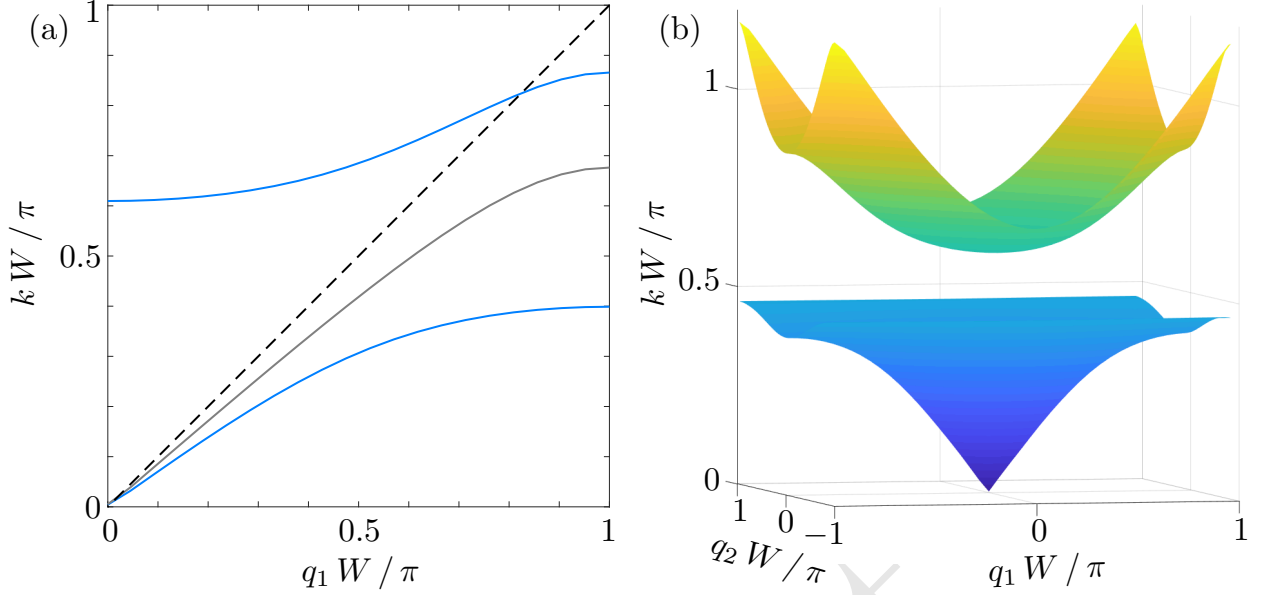
Figure 2: (a) Dispersion curves for $q_2 W = 0$, $a / W = 0.313$ and $\varphi = 0.1\,\pi$ (i.e. C-shaped resonator; blue curves) $\varphi = 0$ (i.e. closed circles; grey), with the light-line overlaid (broken curve). (b) Dispersion surfaces for the C-shaped resonator ($\varphi = 0.1\,\pi$) in the first Brillouin zone.

$= a_5$) are displayed in Figure 2. The left-hand panel shows the first and the second band (solid blue lines) for $q_2 = 0$. In solid-state physics, the left-hand end, $q_1 W = 0$, is called the Γ-point, while the right-hand end, $q_1 W = \pi$, is referred to as the X-point. For comparison, the first band of the equivalent closed circle ($\varphi = 0$, same outer radius) is also shown (solid black line) as well as the so-called light line (dashed black line), which is the band of free space. As can be seen, the presence of the scatterers lowers the wavenumber in comparison to free space and the C-shaped resonators do this much more so than the closed circles. Moreover, a band gap for waves propagating in the x-direction is seen for approximately $k W / \pi \in [0.4, 0.6]$.

In order to investigate the band gap for waves propagating in other directions, the first two dispersion surfaces for the C-shape are plotted for the full first Brillouin zone in the right-hand panel of Figure 2. (As noted above, it would have been sufficient to have the plot for the irreducible Brillouin zone; in particular, the symmetry alluded to above is confirmed by the figure.) The first band goes beyond its value at the X-point and the maximum occurs at the point $(q_1 W, q_2 W) = (\pi, \pi)$, the so-called M-point. Therefore, the all-angle band gap is approximately $k W / \pi \in [0.45, 0.6]$. Note that the resonant wavenumber of the equivalent closed circle is $k W / \pi \approx 0.476$, which induces a cut-off for the first band.

As the C-shapes become smaller in radius, the related resonant wavenumber becomes larger and the cut-off moves up in the band diagram. Accordingly, the first bands of smaller C-shaped-resonator radii go to higher wavenumbers (not shown). Therefore, a gently graded array of C-shaped resonators, where the radius of the C-shapes increases away from the front of the array, is expected to allow waves to penetrate into the array up to the location at which the associated band diagram has a gap for the wavenumber of the incident wave. Note also that the slope of the dispersion curve gives the group velocity of the wave, which is the velocity at which energy propagates. As the slope of the first band is zero at the X-point, the group velocity is zero at this point, causing energy to accumulate.

3 Stacks of infinite diffraction gratings

The key to understanding the effects of grading on a stack of infinite diffraction gratings lies in analysing how the eigenvalues of the transfer matrices for the individual gratings evolve with the grading. In each of the M gratings, the C-shaped resonators are repeated periodically in the $\pm y$-direction, so that they form the columns of the array. Reflection and transmission of a plane incident wave by a single grating is calculated using the method given by, e.g., [7], with the diffraction transfer matrix for a single C-shaped resonator calculated using the method of [8], in which C-shaped resonators are treated as being infinitely thin (i.e. one-dimensional objects). Wave interactions between the gratings in a stack are then calculated using the method developed by [9–11].

We briefly lay out the ideas in the notation of this paper. The scattered solution for a single grating can be expressed as a countable sum of propagating/decaying plane waves. As in the finite-array case introduced in §1, the distance between centres of adjacent C-shaped scatterers is denoted by W, and the incident wave, ϕ_{inc}, propagates towards the array at an angle ψ with respect to the positive x-axis, as in (2). The directions of the scattered waves are determined by the discrete set of real solutions ψ_j of

$$\psi_j = \arcsin(\beta_j), \quad \text{where} \quad \beta_j = \beta + \frac{2\,j\,\pi}{k\,W} \quad \text{for } j \in \mathbb{Z}. \tag{6}$$

The elements of the set $\{\psi_j : j \in \mathbb{Z}\}$ are referred to as the scattering angles. They depend only on the y-periodicity dictated by the incident wave and the spacing W, and are independent of the scatterer properties (i.e. C-shaped resonator properties).

As indicated in (3), the columns (i.e. gratings) are labelled $m = 1, \ldots, M$, and ordered left to right. Column m occupies the x-interval $x_{m-} < x < x_{m+}$, where $x_{m\pm} = x_m \pm W/2$, and the centres of the C-shaped resonators in the column lie on the contour $x = x_m$, noting that $x_{m+} = x_{m+1-}$ for $m = 1, \ldots, M-1$. The wave field between columns m and $m+1$ is

$$\phi(x,y) = \sum_{j=-\infty}^{\infty} a_j^{(m+)}\, \mathrm{e}^{\mathrm{i}\,k\,\{\beta_j\,y + \alpha_j\,(x - x_{m+})\}} + b_j^{(m+)}\, \mathrm{e}^{\mathrm{i}\,k\,\{\beta_j\,y - \alpha_j\,(x - x_{m+})\}}, \tag{7a}$$

$$= \sum_{j=-\infty}^{\infty} b_j^{(m+1-)}\, \mathrm{e}^{\mathrm{i}\,k\,\{\beta_j\,y + \alpha_j\,(x - x_{m+1-})\}} + a_j^{(m+1-)}\, \mathrm{e}^{\mathrm{i}k\,\{\beta_j\,y - \alpha_j\,(x - x_{m+1-})\}}, \tag{7b}$$

where $a_j^{(m\pm)}$ and $b_j^{(m\pm)}$, respectively, are the incoming and outgoing wave amplitudes, from the left $(-)$ and right $(+)$ of column m.

It is convenient to introduce matrix and vector notation at this point. Therefore, following truncation, expression (7) is recast as

$$\phi(x,y) \approx \mathrm{e}^{\mathrm{i}\,k\,\beta\,y}\left(\mathrm{e}^{\mathrm{i}\,k\,\alpha\,(x - x_{m+})}\mathbf{a}_{m+} + \mathrm{e}^{-\mathrm{i}\,k\,\alpha\,(x - x_{m+})}\mathbf{b}_{m+}\right), \tag{8a}$$

$$\approx \mathrm{e}^{\mathrm{i}\,k\,\beta\,y}\left(\mathrm{e}^{\mathrm{i}\,k\,\alpha\,(x - x_{m+1-})}\mathbf{b}_{m+1-} + \mathrm{e}^{-\mathrm{i}\,k\,\alpha\,(x - x_{m+1-})}\mathbf{a}_{m+1-}\right), \tag{8b}$$

using the following notation for diagonal matrices

$$\mathrm{e}^{\mathrm{i}\,k\,\beta\,y} = \mathrm{diag}\{\mathrm{e}^{\mathrm{i}\,k\,\beta_j\,y}\} \quad \text{and} \quad \mathrm{e}^{\pm\mathrm{i}\,k\,\alpha\,x} = \mathrm{diag}\{\mathrm{e}^{\pm\mathrm{i}\,k\,\alpha_j\,x}\},$$

and for vectors

$$\mathbf{a}_{m\pm} = \mathrm{vec}\{a_j^{m\pm}\} \quad \text{and} \quad \mathbf{b}_{m\pm} = \mathrm{vec}\{b_j^{m\pm}\}.$$

The transfer matrix $\mathcal{P}_m$ is the matrix that relates amplitudes on either side of column m, i.e.

$$\begin{pmatrix} \mathbf{b}_+ \\ \mathbf{a}_+ \end{pmatrix} = \mathcal{P}_m \begin{pmatrix} \mathbf{a}_- \\ \mathbf{b}_- \end{pmatrix}. \tag{9}$$
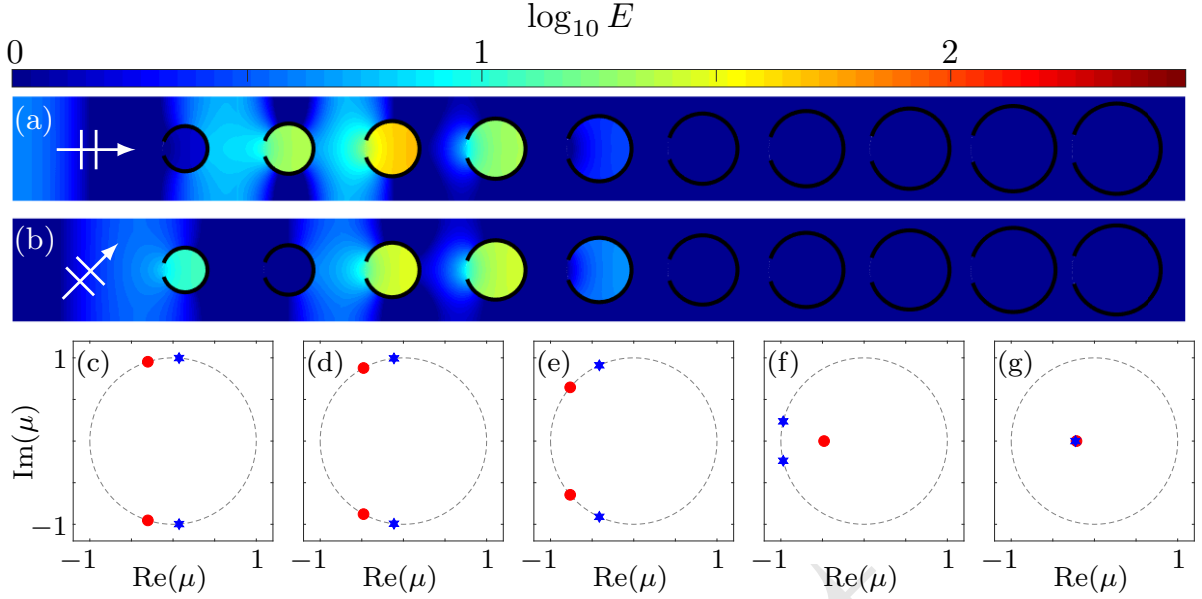
Figure 3: (a) As in Figure 1, but for a single row of a stack of infinite diffraction gratings. (b) Corresponding results for oblique incidence with $\psi = \pi / 4$. (c–g) Dominant eigenvalues of transfer matrices in complex plane, for $\psi = 0$ (red bullets) and $\psi = \pi / 4$ (blue stars) operating over columns $n = 1, \ldots, 5$. The unit circles is overlaid (broken curve).

The eigenvalues of the transfer matrix, $\{\mu \in \mathbb{C} : \mu \in \mathrm{eig}(\mathcal{P}_m)\}$, make up the spectrum of the associated operator, and define the waves supported by the corresponding doubly-periodic array. In particular, eigenvalues on the unit circle, $|\mu| = 1$, define Bloch wavenumbers on the bands via the relation $\mu = \exp(\mathrm{i}\, q_1 W)$, with q_2 defined by the incident wave via $q_2 = k \sin \psi$.

Figure 3(a) shows results analogous to those of Figure 1 but for a single row within a stack of infinite gratings. In this case, the maximum amplification occurs in the third column of C-shaped resonators, $m = 3$, as opposed to the fourth column in Figure 1. The amplification is weaker in the infinite-row array (stack of gratings) than the single-row array shown in Figure 1: it is ≈ 50 times the incident energy and 2.6 times the amplification of the isolated cylinder. Figure 3(b) shows results for an incident wave with angle $\psi = \pi / 4$. The maximum amplification also occurs in the third column but is slightly weaker, at ≈ 30 times the incident energy and 1.6 times the amplification of the isolated cylinder. The amplification is almost the same in the fourth column, indicating that the wave has penetrated farther into the array before reaching the cut-off. The behaviour is consistent with the band diagrams shown in Figure 2, in which, at the M-point, the dispersion surface extends beyond its level at the X-point. (Note that these diagrams are for the fifth C-shape but analogous results hold for the other ones.)

Figures 3(c–g) show the eigenvalues of transfer matrices $\mathcal{P}_m$ for $m = 1$, 2, 3, 4 and 5, respectively, corresponding to the dominant modes in the respective columns. Eigenvalues are shown for $\psi = 0$ (red dots; corresponding to Figure 3a), and for $\psi = \pi/4$ (blue stars; corresponding to Figure 3b). The eigenvalues come in complex-conjugate pairs, with the eigenvalues in the upper-half complex plane defining rightward-propagating waves, and the eigenvalues in the lower-half plane defining leftward-propagating waves.

Figure 3(c) shows the eigenvalues on the unit circle for the transfer matrices that maps over the first column, i.e. there is a single rightward (or leftward) propagating mode supported by the corresponding doubly-periodic array for both $\psi = 0$ and $\psi = \pi / 4$. Figures 3(d–g) shows that as the radius increases along the array columns, the eigenvalues initially move around the unit circle towards -1, with the eigenvalues for $\psi = \pi / 4$ trailing behind those for $\psi = 0$. As the eigenvalues approach -1 from above

(rightward propagating) and below (leftward propagating), the group velocity of the waves reduces, and when the eigenvalues meet at -1 they jump onto the negative real axis, i.e. the associated modes cut-off and decay with no energy propagation; one eigenvalue jumps inside the unit circle (rightward decaying), and the other outside (leftward decaying; beyond axes limits). The eigenvalues for $\psi = 0$ cut-off in column 4, whereas the eigenvalues for $\psi = \pi/4$ cut-off in column 5. Therefore, the energy carried by the wave modes accumulate around the third to fourth columns, thereby generating the amplifications shown in Figures 3(a–b). As the eigenvalues for $\psi = \pi/4$ take an additional column to reach the cut-off, the amplification is spread more evenly over columns $m = 3$ to 4. The behaviour is qualitatively similar to the single-row case shown by [1], in which the eigenvalue that jumps off the unit circle onto the negative real axis is associated with the so-called Rayleigh–Bloch mode.

4 Finite arrays

We consider stacks of finite gratings, in which the gratings are truncated after a finite number of C-shapes (symmetrically about the x-axis). This provides an intermediate situation between the columns containing a single C-shaped resonator (as in Figure 1) and an infinite grating (as in §3). The analysis can be performed in a similar fashion to the infinite gratings in § 3 but the reduction to a finite number of resonators in the column complicates the situation. In particular, waves can propagate in all directions for the finite grating, which means that the analogue of the transfer matrix from the §3 is an operator acting on a continuum of directions. The number of discrete eigenvalues is broadly related to the number of members in the column. This directly relates to the transfer-matrix method recently presented in [12], which in turn is based on [13, 14]. We briefly summarise the essence of the method in what follows. A version of this method for a single resonator was used by [1] to analyse the results of Figure 1.

Consider column m, which occupies the region

$$\{(x,y) : x_{m-} < x < x_{m+} \text{ and } y \in \mathbb{R}\}. \tag{10}$$

Outside of the resonators, the total wave field, ϕ, is decomposed into fields propagating/decaying rightwards and leftwards on the left- and right-hand sides of the source via the integral representations

$$\phi(x,y) = \int_{\Gamma_\pm} A_{m\pm}(\chi)\,\varphi_{m\pm}(x,y:\chi)\,\mathrm{d}\chi + \int_{\Gamma_\mp} B_{m\pm}(\chi)\,\varphi_{m\pm}(x,y:\chi)\,\mathrm{d}\chi, \tag{11}$$

where

$$\varphi_\pm(x,y:\chi) = \mathrm{e}^{\mathrm{i}\,k\,\{(x-x_{m\pm})\cos\chi + y\sin\chi\}} \tag{12}$$

is a plane wave travelling in direction χ and normalised to the left-hand side $(-)$ or right-hand side $(+)$ of the column. The integration contours are defined by

$$\Gamma_- = \{-\pi/2 + \mathrm{i}\gamma : \gamma \in \mathbb{R}_+\} \cup \{\gamma \in \mathbb{R} : -\pi/2 \leq \gamma \leq \pi/2\} \cup \{\pi/2 - \mathrm{i}\gamma : \gamma \in \mathbb{R}_+\}, \tag{13}$$

and $\Gamma_+ = \Gamma_- + \pi$. On the real branches of $\Gamma_\pm$, $\varphi_{m\pm}$ defines rightward-propagating waves for Γ_- and leftward-propagating waves for Γ_+. On the complex branches, $\varphi_{m\pm}$ defines plane waves that decay rightwards for Γ_- and leftwards for Γ_+. Note that (11) for $+$ is the analogue of (7) but for a continuum of propagation angles.

In (11), $A_{m\pm}$ and $B_{m\pm}$ represent incoming and outgoing amplitude functions, respectively. The outgoing amplitude functions are expressed in terms of the incoming amplitude functions using the scattering relations

$$B_{m-}(\chi) = \int_{\Gamma_-} R_m(\chi:\psi) A_{m-}(\psi)\,\mathrm{d}\psi + \int_{\Gamma_+} T_m(\chi:\psi) A_{m+}(\psi)\,\mathrm{d}\psi \tag{14a}$$
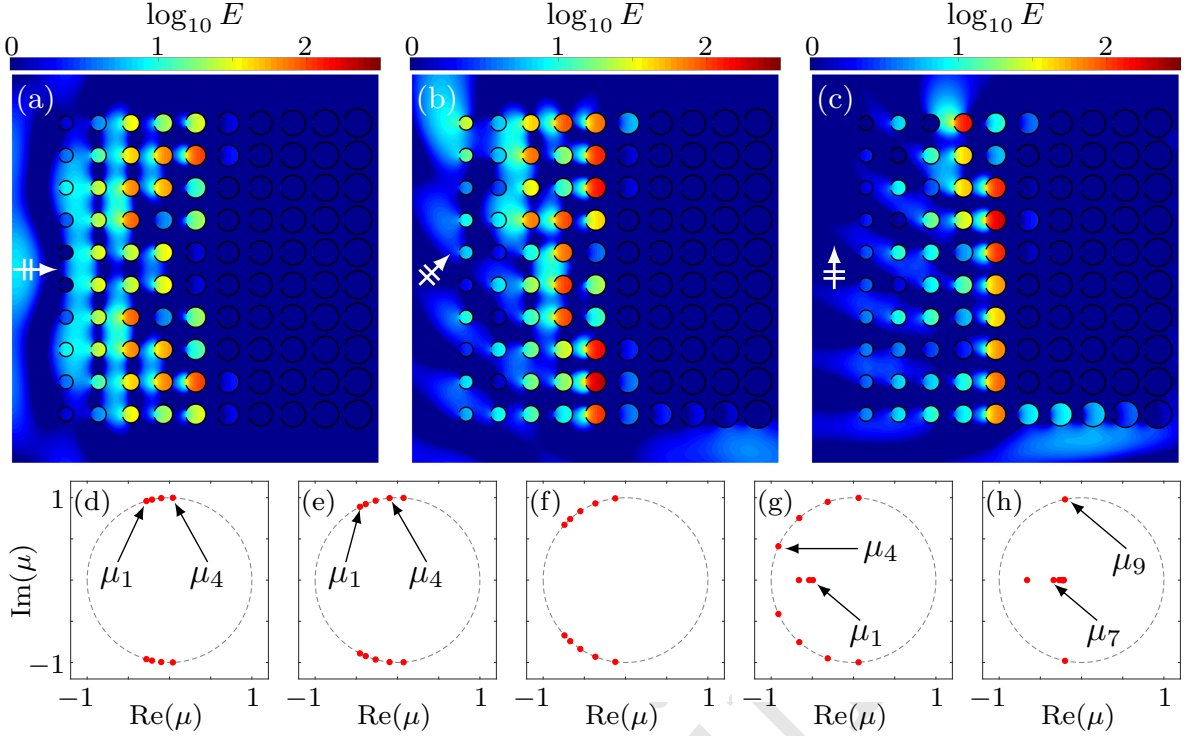
7

Figure 4: (a) As in Figure 1 but for ten rows ($N = 10$). (b) As in (a) but for $\psi = \pi/4$. (c) As in (a) but for $\psi = \pi/2$. (d–h) Eigenvalues of transfer matrices corresponding to point spectrum of columns $m = 1, \ldots, 5$.

$$\text{and} \quad B_{m+}(\chi) = \int_{\Gamma_-} T_m(\chi : \psi) A_{m-}(\psi) \, \mathrm{d}\psi + \int_{\Gamma_+} R_m(\chi : \psi) A_{m+}(\psi) \, \mathrm{d}\psi. \tag{14b}$$

Here, R_m and T_m are, respectively, the reflection and transmission kernels for column m. They determine the outgoing amplitude response in direction χ due to an incoming amplitude forcing in direction ψ.

Denoting the associated integral operators by calligraphic letters,

$$\mathcal{R}_{m\pm} \bullet (\chi) = \int_{\Gamma_\pm} R_m(\chi; \psi) \bullet (\psi) \, \mathrm{d}\psi \quad \text{and} \quad \mathcal{T}_{m\pm} \bullet (\chi) = \int_{\Gamma_\pm} T_m(\chi; \psi) \bullet (\psi) \, \mathrm{d}\psi. \tag{15}$$

The transfer operator is now precisely the operator mapping the amplitude functions from the left boundary of the column across to the right boundary, i.e.

$$\begin{pmatrix} B_{m+} \\ A_{m+} \end{pmatrix} = \mathcal{P}_m \begin{pmatrix} A_{m-} \\ B_{m-} \end{pmatrix} \text{and} \qquad \mathcal{P}_m = \begin{pmatrix} \mathcal{T}_{m-} - \mathcal{R}_{m+}\mathcal{T}_{m+}^{-1}\mathcal{R}_{m-} & \mathcal{R}_{m+}\mathcal{T}_{m+}^{-1} \\ \mathcal{T}_{m+}^{-1}\mathcal{R}_{m-} & \mathcal{T}_{m+}^{-1} \end{pmatrix}. \tag{16}$$

Note the close similarity of (16) to (9). However, (9) is a relation for a discrete number of scattering angles, while (16) is a relation for a continuum of directions and is independent of the incident field, as there is no imposed quasi-periodicity, i.e. no q_2. Relation (16) becomes a finite-dimensional matrix relation after discretisation (and truncation) of the complex contours $\Gamma_\pm$.

Figures 4(a–c) show spatial energy distributions for a graded array of 10×10 C-shaped resonators, in which each column is made up of ten identical resonators of the type shown in Figure 1, and for (a) normal incidence $\psi = 0$, (b) oblique incidence $\psi = \pi/4$ and (c) grazing incidence $\psi = \pi/2$. For normal incidence, the maximum energy amplification is approximately 104 times the incident energy, which is more than twice the maximum amplification in the corresponding infinite array. The

8

maximum occurs in the fifth column and the second and ninth rows (counted from the top), i.e. for cylinders that resonate in isolation for the chosen incident wavenumber; the amplifications are 1.8 times greater than for the cylinders in isolation. Large amplifications also occur in the third column and the fourth and seventh row, for which the energy amplifications are ≈ 87 times the incident wave energy and 4.6 times the amplifications in the isolated cylinders, and the third and sixth rows and the fourth column in rows two and nine, for which the amplifications are ≈ 70 times the incident wave and 1.7 times the isolated cylinders. Hardly any energy reaches the sixth column (maximum amplification of about 2 occurring in rows two and nine), and virtually none in columns farther into the array. Boundary effects are clearly visible at the upper and lower edge of the array. For both oblique and grazing incidence, the amplification patterns are broadly similar, with cut-offs after the fifth column. The energy amplifications are generally larger: up to > 210 times the incident wave energy for $\psi = \pi/4$ and > 185 for $\psi = \pi/2$. Note that, for a single row ($N = 1$), as in Fig. 1, the discrete spectrum contains a single eigenvalue corresponding to the Rayleigh–Bloch wave [1], which cannot be excited at grazing incidence due to symmetry arguments.

Figures 4(d–h) show eigenvalues of the transfer matrices $\mathcal{P}_m$ for $m = 1, \ldots, 5$, respectively. In contrast to the eigenvalues for infinite gratings shown in Figures 3(c–g), the eigenvalues for finite gratings are the same for normal and oblique incidence. Only the point eigenvalues are shown; for the first column (smallest resonators), there are four eigenvalues on the unit circle in the upper-half plane (and four in the lower-half plane), which are fractionally displaced along from the ends of the continuous spectrum (the numerical approximation of which is omitted for clarity in the plots). The eigenvalue farthest away from the continuous spectrum is labelled μ_1 and closest is μ_4, as shown in Figure 4(d). In a similar fashion to the eigenvalues of the infinite grating shown in Figures 3(c–g), as the resonators get larger from $m = 1$ to 5, the eigenvalues move around the unit circle towards -1 before jumping onto to the negative real line; the locations of μ_1 and μ_4 for the second and fourth columns are indicated on Figures 4(e) and (g), respectively. Therefore, analogous conclusions about the cut-off of modes for the infinite gratings in §3, can be drawn for the finite array. However, the behaviour is more complicated for the finite array, because (i) there are more (point) eigenvalues (although not all of the modes corresponding to the eigenvalues are shown due to the symmetry of the incident field with respect to the array), and (ii) additional eigenvalues appear from the ends of the continuous spectrum as the resonators get larger, with five eigenvalues in the upper-half place for column $m = 2$, and nine in the upper-half complex plane/on the negative real axis within the unit circle for column $m = 5$. This leads to non-uniform response in the different rows for normal incidence, and maximum amplifications appearing in different rows along the array.

In order to gain further insight into the resonant behaviour, Figure 5 shows energy amplifications of the projections of the wavefield in columns $m = 4$ and 5 onto the most strongly excited modes $\mathcal{M}_j$ for normal incidence shown in Figure 4(a), associated with the eigenvalues μ_j labelled in Figures 4(d,h). In the fourth column, $\mathcal{M}_1$ is the dominant mode, followed closely by $\mathcal{M}_4$, and the left-hand and middle panels of Figure 5(a) show their respective contributions to the wavefield. Mode $\mathcal{M}_1$ has cut-off in the fourth column, and $\mathcal{M}_4$ is the next mode to cut-off after the fourth column. The right-hand panel of Figure 5(a) shows the sum of all modes combined, $\sum_1^7$, where the sum includes the contributions of the leftward propagating decaying modes in the point spectrum. from which the dominance of $\mathcal{M}_1$ and $\mathcal{M}_4$ is clearly seen. Figure 5(b) shows analogous results for the fifth column of the array, in which the dominant modes are $\mathcal{M}_7$ and $\mathcal{M}_9$, with $\mathcal{M}_7$ having cut-off in the fifth column and $\mathcal{M}_9$ about to cut-off. Again, it is clearly seen from these plots that the response in the column is dominated by these modes.

5   Conclusions

Two-dimensional square-lattice resonator arrays, in which the resonator radii are graded with distance from the front of the array, have been shown to generate large energy amplifications at certain locations
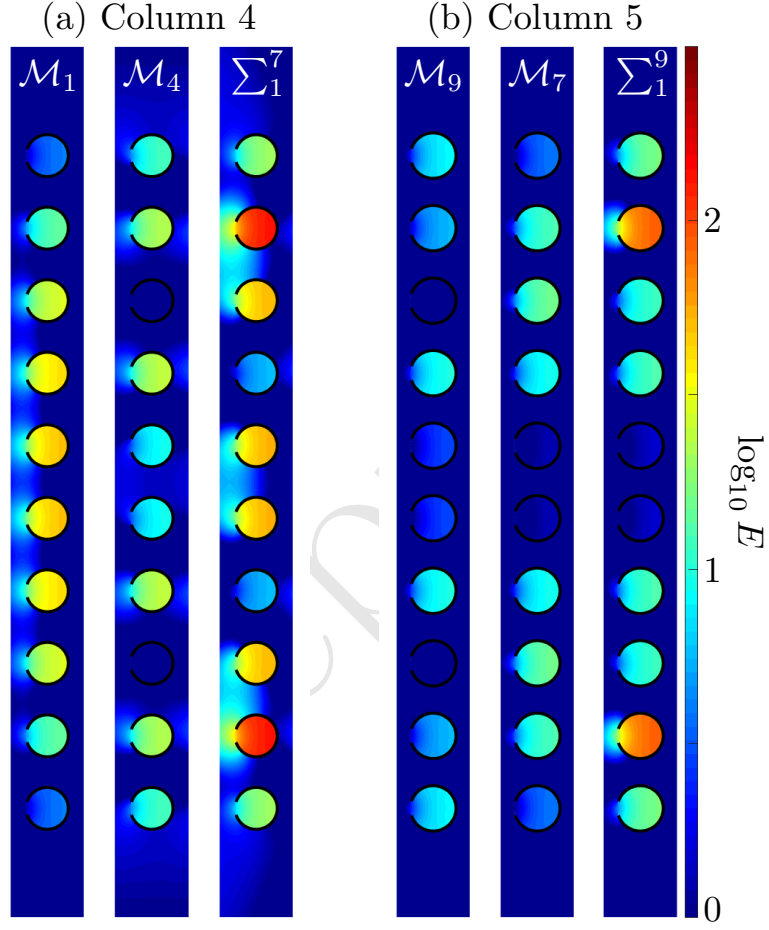
Figure 5: Left-hand and middle panels show normalised logarithmic energy supported by the two dominant modes excited by a normally incident wave, as shown in Figure 4(a), for (a) column $m = 4$ and (b) column $m = 5$. Right-hand panels show combined contribution of all modes corresponding to discrete spectrum.

in the array. Understanding of the amplification locations was derived by treating the array as a stack of diffraction gratings, and analysing the locations along the array at which the modes associated to eigenvalues of the transfer matrices acting over the individual gratings cut-off. It was shown that the maximum amplifications are larger for finite arrays than infinite arrays, but that the amplification patterns are more complicated for finite arrays. The complicated amplification pattern was related to excitation of multiple modes corresponding to point eigenvalues, with different cut-off locations along the array.

References

[1] L. G. Bennetts, M. A. Peter, and R. V. Craster. Graded resonator arrays for spatial frequency separation and amplification of water waves. *J. Fluid Mech.*, 854, 2018. doi: 10.1017/jfm.2018.648.

[2] K. L. Tsakmakidis, A. D. Boardman, and O. Hess. Trapped rainbow storage of light in metamaterials. *Nature*, 450:397–401, 2007.

[3] N. Jiménez, V. Romero-García, V. Pagneux, and J.-P. Groby. Rainbow-trapping absorbers: Broadband, perfect and asymmetric sound absorption by subwavelength panels for transmission problems. *Sci. Rep.*, 7:13595, 2017.

[4] D.J. Colquitt, A. Colombi, R.V. Craster, P. Roux, and S.R.L. Guenneau. Seismic metasurfaces: Sub-wavelength resonators and rayleigh wave interaction. *J. Mech. Phys. Solids*, 99(6):379–393, 2017.

[5] M. Jang and H. Atwater. Plasmonic rainbow trapping structures for light localization and spectrum splitting. *Phys. Rev. Lett.*, 107:207401, 2011.

[6] V. Romero-Garcia, R. Pico, A. Cebrecos, V. J. Sanchez-Morcillo, and K. Staliunas. Enhancement of sound in chirped sonic crystals. *Appl. Phys. Lett.*, 102:091906, 2013.

[7] M. A. Peter, M. H. Meylan, and C. M. Linton. Water-wave scattering by a periodic array of arbitrary bodies. *J. Fluid Mech.*, 548:237–256, 2006.

[8] F. Montiel, H. Chung, M. Karimi, and N. Kessissoglou. An analytical and numerical investigation of acoustic attenuation by a finite sonic crystal. *Wave Motion*, 70:135–151, 2017.

[9] M. A. Peter and M. H. Meylan. Water-wave scattering by vast field of bodies. *SIAM J. Appl. Math.*, 70(5):1567–1586, 2009.

[10] L. G. Bennetts and V. A. Squire. Wave scattering by multiple rows of circular ice floes. *J. Fluid Mech.*, 639:213–238, 2009. doi: 10.1017/S0022112009991017.

[11] L. G. Bennetts and M. A. Peter. Spectral analysis of wave propagation through rows of scatterers via random sampling and a coherent potential approximation. *SIAM J. Appl. Math.*, 73(4): 1613—1633, 2013.

[12] L. G. Bennetts, M. A. Peter, and F. Montiel. Localisation of Rayleigh–Bloch waves and damping of resonant loads on arrays of vertical cylinders. *J. Fluid Mech.*, 813:508–527, 2017. doi: 10.1017/jfm.2016.855.

[13] F. Montiel, V. A. Squire, and L. G. Bennetts. Evolution of directional wave spectra through finite regular and randomly-perturbed arrays of scatterers. *SIAM J. Appl. Math.*, 75:630–651, 2015. doi: 10.1137/140973906.

[14] F. Montiel, V. A. Squire, and L. G. Bennetts. Attenuation and directional spreading of ocean wave spectra in the marginal ice zone. *J. Fluid Mech.*, 790:492–522, 2016. doi: 10.1017/jfm.2016.21.